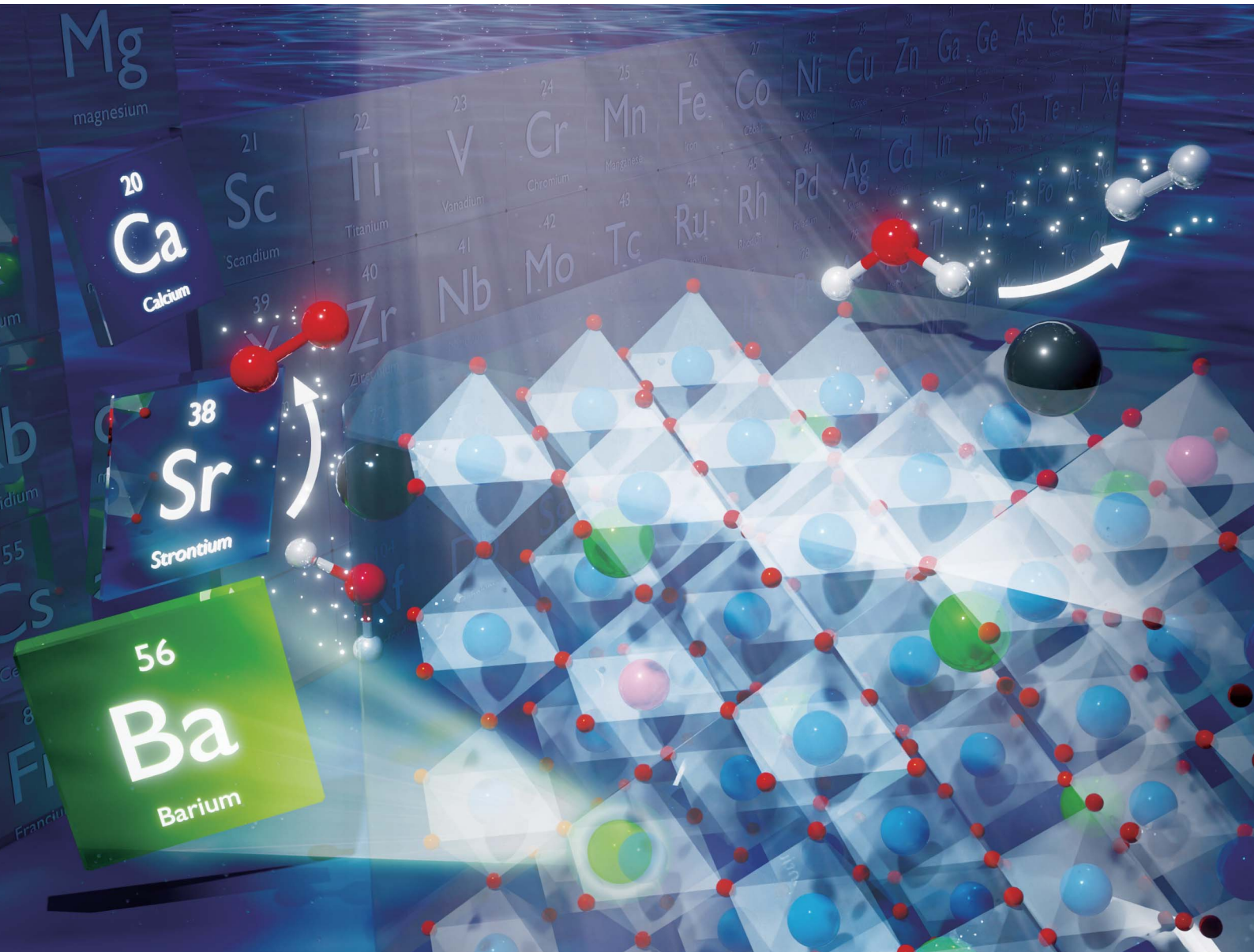


Sustainable Energy & Fuels

Interdisciplinary research for the development of sustainable energy technologies

rsc.li/sustainable-energy



ISSN 2398-4902



Cite this: *Sustainable Energy Fuels*, 2025, 9, 6665

Activation of barium titanate for photocatalytic overall water splitting *via* low-valence cation codoping

Shigeru Ikeda, ^{a,b} Kaori Takagi, ^a Ryota Tomizawa, ^c Tomoya Nagano, ^c Koji Hayashi, ^c Akira Yamakata ^d and Yoshitaro Nose ^e

Barium titanate (BaTiO_3) has long been regarded as inactive for photocatalytic overall water splitting, in stark contrast to its perovskite counterparts SrTiO_3 and CaTiO_3 . Here we report that BaTiO_3 codoped with Al^{3+} and Sc^{3+} at Ti^{4+} sites under flux synthesis conditions is activated as a robust photocatalyst for overall water splitting. This material achieves apparent quantum yields of 29.8% at 310 nm and 27.5% at 365 nm, representing the first demonstration of efficient overall water splitting on BaTiO_3 . Comparative analyses show that BaTiO_3 doped only with Al^{3+} suffers from severe band-edge disorder, whereas BaTiO_3 codoped with Al^{3+} and Mg^{2+} exhibits clear activation with moderate efficiency. In contrast, BaTiO_3 codoped with Al^{3+} and Sc^{3+} achieves the critical defect and structural control required to push the material across the threshold from inactive to highly active. These findings overturn the long-standing perception of BaTiO_3 as unsuitable for water splitting and establish a general design principle for activating previously inactive perovskite oxides, thereby expanding the materials palette for solar-to-hydrogen energy conversion.

Received 7th October 2025
Accepted 21st October 2025

DOI: 10.1039/d5se01323b
rsc.li/sustainable-energy

Introduction

Photocatalytic overall water splitting using semiconductor oxides has long been studied as a promising route for sustainable hydrogen (H_2) production from sunlight.¹ Among perovskite-type oxides, strontium titanate (SrTiO_3) has been the most extensively investigated and has emerged as a benchmark photocatalyst.² Recent studies have demonstrated that SrTiO_3 can achieve an apparent quantum yield (AQY) approaching unity under monochromatic ultraviolet (UV) irradiation at 365 nm, enabled by a bulk structural modification through flux treatment and Al^{3+} doping, together with optimized cocatalyst loading.³ Moreover, SrTiO_3 photocatalysts have been scaled up to 100 m^2 -class modules for pilot demonstrations of solar H_2 production.⁴ Al^{3+} has been regarded as an essential dopant, acting both as a p-type dopant to compensate surplus electrons generated by oxygen vacancies and as a promoter of specific crystal facets critical for overall water splitting.^{3,5} More recently, we demonstrated that

highly active SrTiO_3 photocatalysts can also be realized without Al^{3+} , by employing codoping with Mg^{2+} and Sc^{3+} in place of Al^{3+} .⁶ In addition, visible-light-responsive SrTiO_3 -based photocatalysts have also been achieved by doping transition-metal cations such as Cr^{3+} , Ir^{3+} , and Rh^{3+} ,⁷ and their application in Z-scheme two-step water splitting systems has enabled solar-to- H_2 (STH) efficiencies as high as 1%, a value still unattainable in one-step photocatalyst systems.⁸

Another perovskite oxide, calcium titanate (CaTiO_3), with Ca^{2+} occupying the A-site, has also been studied for photocatalytic reactions including overall water splitting.⁹ Although its application dates back several decades, the activity had long remained modest compared with SrTiO_3 . By applying our codoping strategy, however, we significantly improved its photocatalytic activity and achieved an AQY exceeding 70% at 310 nm.¹⁰ Visible-light response was further realized by Rh^{3+} doping,¹¹ expanding the scope of CaTiO_3 photocatalysts.

In contrast, barium titanate (BaTiO_3), another perovskite titanate with Ba^{2+} at the A-site, is well known for its ferroelectric, dielectric, and piezoelectric properties,¹² but has been regarded as unsuitable for overall water splitting. Only a limited number of studies have examined BaTiO_3 in this context,¹³ and the material has consistently shown negligible activity. Inoue *et al.*, in their early studies on related titanates in the 1990s, explicitly noted BaTiO_3 as inactive, while reporting that BaTi_4O_9 , a phase composed of the same elements, exhibited water-splitting activity.¹⁴ Subsequent optimization of BaTi_4O_9 , moreover, achieved an AQY of 41% at 313 nm.¹⁵ To date, however, no report

^aFaculty of Science and Engineering, Konan University, 8-9-1 Okamoto, Higashinada-ku, Kobe, Hyogo 658-8501, Japan

^bInstitute for Energy Conversion Materials, Konan University, 8-9-1 Okamoto, Higashinada-ku, Kobe, Hyogo 658-8501, Japan

^cCarbon Neutral Energy Development Division, Toyota Motor Corporation, 1200 Mishuku, Susono, Shizuoka 410-1193, Japan

^dResearch Institute for Interdisciplinary Science, Okayama University, 3-1-1 Tsushima-naka, Kita-ku, Okayama 700-8530, Japan

^eDepartment of Materials Science and Engineering, Kyoto University, Yoshida Honmachi, Sakyo-ku, Kyoto, 606-8501, Japan



has demonstrated efficient overall water splitting using BaTiO_3 , which has fundamentally hindered its consideration as a viable photocatalyst.

Herein, we demonstrate for the first time that BaTiO_3 can be activated as an efficient photocatalyst for overall water splitting through low-valence cation codoping under flux conditions. While Al^{3+} doping alone, which is effective in SrTiO_3 and CaTiO_3 , proved insufficient in BaTiO_3 , codoping with Al^{3+} and Sc^{3+} or with Al^{3+} and Mg^{2+} led to a significant enhancement in photocatalytic activity. Among these, the BaTiO_3 sample codoped with Al^{3+} and Sc^{3+} exhibited the highest performance, achieving AQYs of 29.8% at 310 nm and 27.5% at 365 nm. These results overturn the long-standing perception of BaTiO_3 as an inactive material and establish a design principle for activating previously unsuitable perovskite oxides, thereby expanding the materials palette for solar-driven H_2 production.

Experimental

Materials

All chemicals were reagent grade ($\geq 99\%$) or higher and used without further purification.

Synthesis of BaTiO_3 powders

Non-doped BaTiO_3 powder was prepared *via* a conventional solid-state reaction (SSR). A stoichiometric mixture of BaCO_3 and TiO_2 was ground in an agate mortar and heated at $1000\text{ }^\circ\text{C}$ for 10 h in air. Doped BaTiO_3 powders were synthesized by flux treatment of the obtained BaTiO_3 powder together with dopant source oxides (Al_2O_3 , Sc_2O_3 , or MgO) in molten BaCl_2 (1000 mol% relative to BaTiO_3) at $1050\text{ }^\circ\text{C}$ for 10 h in an alumina crucible (Nikkato, 99.6%). The nominal contents of dopant cations (Al^{3+} , Sc^{3+} , or Mg^{2+}) were fixed at 1.0 mol% relative to Ti^{4+} . After the reaction, the resulting powders were washed repeatedly with deionized water until no Cl^- was detected (confirmed by AgNO_3 test) and dried at $70\text{ }^\circ\text{C}$ in a convection oven. For comparison, flux treatment of non-doped BaTiO_3 powder without intentional dopant addition was performed; this yielded BaTiO_3 powder containing trace Al^{3+} due to elution from the alumina crucible.

Cocatalyst loading

For loading of $\text{Rh/Cr}_2\text{O}_3$ and CoOOH cocatalysts, 100 mg of the doped BaTiO_3 powder was dispersed in 100 mL of distilled water in a cylindrical glass vessel (diameter 50 mm, height 70 mm) with a quartz window. The suspension was stirred magnetically during irradiation with a 300 W Xe lamp (CERMAX PE300BF) positioned at a distance of 15 cm from the liquid surface. Aqueous precursor solutions of $\text{RhCl}_3 \cdot 3\text{H}_2\text{O}$, K_2CrO_4 , and $\text{Co}(\text{NO}_3)_2 \cdot 6\text{H}_2\text{O}$ were sequentially added to deposit 0.1 wt% Rh, 0.05 wt% Cr, and 0.05 wt% Co, respectively. The deposition times were 10 min for Rh, and 5 min each for Cr_2O_3 and CoOOH , all under continuous light irradiation.

Alternatively, loading of mixed Rh–Cr oxide ($(\text{Rh},\text{Cr})_2\text{O}_3$) was carried out by the impregnation method.⁴ Precursor solutions of $\text{RhCl}_3 \cdot 3\text{H}_2\text{O}$ and K_2CrO_4 were added to 100 mg of each BaTiO_3

sample, followed by drying at $70\text{ }^\circ\text{C}$ and subsequent mild heating at $300\text{ }^\circ\text{C}$ for 1 h in air to form $(\text{Rh},\text{Cr})_2\text{O}_3$.

Photocatalytic overall water splitting

Photocatalytic reactions were carried out in the same quartz-windowed vessel connected to a closed, air-free gas circulation and analysis system. The reaction suspension (100 mg photocatalyst in 100 mL pure water) was thoroughly degassed by evacuation and backfilled with argon (Ar, 99.999%) to *ca.* 20 kPa prior to irradiation. The photocatalyst was irradiated using a 300 W Xe lamp (CERMAX PE300BF) through a cold mirror that mainly reflects UV light, thereby providing UV/near-UV irradiation (<500 nm) to the suspension. Evolved H_2 and molecular oxygen (O_2) were analyzed using a GL Sciences GC3210 gas chromatograph equipped with a thermal conductivity detector (TCD) and an MS-5A column, with Ar as the carrier gas.

Characterization

The actual molar compositions of the samples were determined by inductively coupled plasma (ICP) analysis (Shimadzu ICPS-8100). Crystallographic structures were determined by powder X-ray diffraction (XRD, PANalytical X'Pert PRO Alpha-1 diffractometer) equipped with a Johansson-type curved Ge(111) monochromator, using monochromatic $\text{Cu K}\alpha_1$ radiation ($\lambda = 0.15406\text{ nm}$). Raman spectra were measured using a JASCO NRS-3100 laser Raman spectrometer with an excitation wavelength of 532 nm. Particle morphologies were observed using a JEOL JSM-IT800 scanning electron microscope (SEM). UV-vis diffuse reflectance spectra (DRS) were obtained with a Shimadzu UV-2600i spectrophotometer equipped with an ISR-2600Plus integrating sphere. The specific surface areas of the samples were measured using a BELSORP MAX X gas adsorption–desorption analyzer at 77 K with Kr as the adsorbate gas. Samples were degassed under vacuum at $150\text{ }^\circ\text{C}$ for 5 h prior to measurement.

AQY measurements

AQY was estimated from the H_2 evolution rate and the incident photon flux per unit time using the following equation:

$$\text{AQY} (\%) = \{(N_{\text{H}_2} \times 2)/N_{\text{p}}\} \times 100 \quad (1)$$

where N_{H_2} is the number of evolved H_2 and N_{p} is the number of incident photons that reached the surface of the reaction solution. The factor of 2 accounts for the two electrons required to generate one H_2 molecule. Monochromatic irradiation for this measurement was performed using a Hamamatsu Photonics LC8 high-pressure mercury (Hg) lamp equipped with bandpass filters (Asahi Spectra, $310 \pm 5\text{ nm}$ or $365 \pm 5\text{ nm}$). The incident photon flux was determined using a calibrated silicon photodiode power meter.

Results and discussion

Photocatalytic activity of BaTiO_3 -based samples

BaTiO_3 -based photocatalysts with different dopant compositions were examined for overall water splitting. In this study, the



samples are denoted as follows: $\text{BaTiO}_3:\text{Al}$ (flux-treated BaTiO_3 containing Al^{3+} eluted from the alumina crucible), $\text{BaTiO}_3:\text{Al},\text{Al}$ (intentionally Al^{3+} -doped BaTiO_3 further containing crucible-derived Al^{3+}), $\text{BaTiO}_3:\text{Al},\text{Sc}$ (codoped with crucible-derived Al^{3+} and intentionally added Sc^{3+}), and $\text{BaTiO}_3:\text{Al},\text{Mg}$ (codoped with crucible-derived Al^{3+} and intentionally added Mg^{2+}). All samples were loaded with $\text{Rh}/\text{Cr}_2\text{O}_3$ and CoOOH cocatalysts *via* photo-deposition method, and their activities for H_2 and O_2 evolution were evaluated under UV irradiation. Fig. 1a summarizes the photocatalytic activities of these BaTiO_3 -based samples, presented as the rates of H_2 and O_2 evolution ($\mu\text{mol h}^{-1}$). As in previous reports,¹⁴ BaTiO_3 prepared by solid-state reaction (SSR) exhibited only slight H_2 evolution with no detectable O_2 generation, even when loaded with highly active cocatalysts, confirming that pristine BaTiO_3 is below the threshold for overall water splitting. Unlike SrTiO_3 , where Al^{3+} doping under flux conditions markedly enhances activity, the $\text{BaTiO}_3:\text{Al}$ and $\text{BaTiO}_3:\text{Al},\text{Al}$ samples showed no improvement; their H_2 evolution rates were even lower than those of pristine BaTiO_3 , suggesting that Al^{3+} addition alone introduces unfavourable structural and electronic effects that hinder efficient carrier utilization.

When Sc^{3+} or Mg^{2+} was introduced together with crucible-derived Al^{3+} during flux treatment, a significant enhancement in photocatalytic activity was achieved. In particular, $\text{BaTiO}_3:\text{Al},\text{Sc}$ exhibited the highest activity, with H_2 and O_2 evolution

rates approaching stoichiometric ratios. $\text{BaTiO}_3:\text{Al},\text{Mg}$ also showed clear activation, though with somewhat lower efficiency. These results demonstrate that codoping allows BaTiO_3 to overcome its long-standing activity threshold, providing the first clear evidence that this material can function as an efficient photocatalyst for overall water splitting. The time course of H_2 and O_2 evolution for $\text{BaTiO}_3:\text{Al},\text{Sc}$ under continuous UV irradiation is shown in Fig. 1b. Over at least five runs, corresponding to 15 h of irradiation, the gas evolution rates remained essentially unchanged, demonstrating the durability and steady-state performance of the $\text{BaTiO}_3:\text{Al},\text{Sc}$ photocatalyst.

To verify that these differences in activity do not arise from the cocatalyst deposition method, $(\text{Rh},\text{Cr})_2\text{O}_3$ was also deposited by an impregnation method,⁴ and photocatalytic tests were performed under identical conditions. As shown in Fig. S1, the same relative trend was reproduced, confirming that the observed activity enhancement originates from the intrinsic bulk and surface properties of the BaTiO_3 host materials. Notably, in these comparative tests, CoOOH was not deposited as an O_2 -evolution cocatalyst. As a result, $\text{BaTiO}_3:\text{Al},\text{Mg}$ exhibited detectable H_2 evolution, whereas O_2 remained below the detection limit. This deviation from stoichiometric gas evolution therefore arises primarily from the absence of CoOOH , which limits the kinetics of water oxidation, rather than from any intrinsic inactivity of the $\text{BaTiO}_3:\text{Al},\text{Mg}$ sample itself.

Structural, optical, and morphological properties

The dopant concentrations determined by ICP analysis are summarized in Table 1. In line with previous reports on SrTiO_3 and CaTiO_3 ,^{3–6,10} appreciable amounts of Al^{3+} (*ca.* 0.4–0.7%) originating from the dissolution of the alumina crucible were detected in all samples. However, the Al^{3+} content in intentionally doped samples was nearly identical to that in $\text{BaTiO}_3:\text{Al}$, which contained only crucible-derived Al^{3+} . This result indicates that, unlike SrTiO_3 and CaTiO_3 , substitution of Al^{3+} (0.0535 nm, CN = 6) for Ti^{4+} (0.0605 nm, CN = 6) is strongly hindered in BaTiO_3 ,¹⁶ likely due to its relatively large lattice constant and the resulting size mismatch that prevents effective incorporation at the B-site. In contrast, dopants with larger ionic radii than Ti^{4+} , such as Mg^{2+} (0.0720 nm, CN = 6) and Sc^{3+} (0.0745 nm, CN = 6),¹⁶ were incorporated at significant levels, with Sc^{3+} showing nearly quantitative incorporation, highlighting its high compatibility with the BaTiO_3 lattice.

X-ray diffraction (XRD) patterns of the BaTiO_3 -based samples exhibited sharp reflections characteristic of tetragonal BaTiO_3 with no detectable impurity phases, as shown in Fig. 2. All values deviated by at most 0.2% from those of the ICDD PDF04-013-5890 reference ($a = b = 0.3995$ nm, $c = 0.4039$ nm), indicating that the lattice constants of the doped samples were essentially unchanged from undoped BaTiO_3 . This suggests that, within the present doping range, the incorporated ions did not significantly affect the average lattice dimensions. Nevertheless, the tetragonal structure was preserved in all cases, and no phase transition to cubic or hexagonal polymorphs was observed. Taken together with the above ICP results, these findings imply that the differences in photocatalytic activity

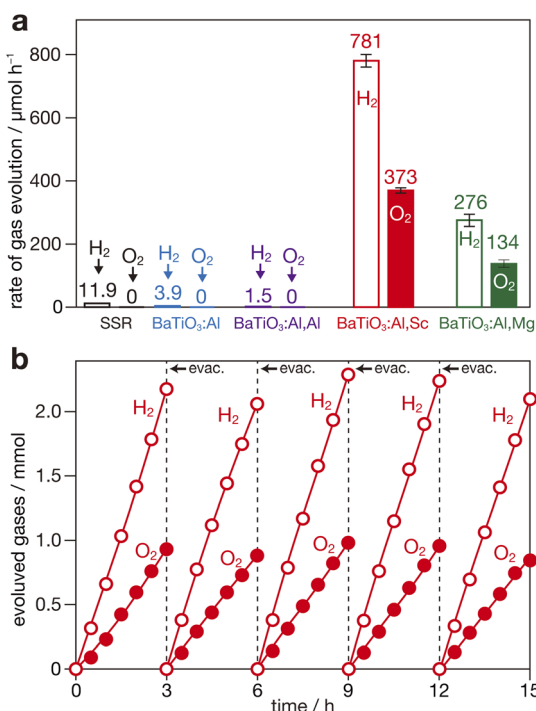


Fig. 1 (a) H_2 and O_2 evolution rates of photocatalysts based on BaTiO_3 prepared by solid-state reaction (SSR), $\text{BaTiO}_3:\text{Al}$, $\text{BaTiO}_3:\text{Al},\text{Al}$, $\text{BaTiO}_3:\text{Al},\text{Sc}$, and $\text{BaTiO}_3:\text{Al},\text{Mg}$ under UV irradiation (<500 nm, 300 W Xe lamp). Error bars represent the standard deviation from at least three independent runs. (b) Time course of H_2 and O_2 evolution over $\text{BaTiO}_3:\text{Al},\text{Sc}$ -based photocatalyst. The reaction system was evacuated every 3 h.



Table 1 Structural, compositional, spectroscopic, and surface properties of flux-treated BaTiO_3 -based samples

Sample	Dopant content ^a /mol%		Lattice constant ^b /nm			FWHM ^c /cm ⁻¹	SA ^d /m ² g ⁻¹
	Al	Sc	Mg	a, b	c		
BaTiO_3 :Al	0.46		Trace ^e	3.988	4.032	10.4	1.1
BaTiO_3 :Al,Al	0.43		Trace ^e	3.991	4.035	10.7	1.6
BaTiO_3 :Al,Sc	0.55	0.94	Trace ^e	3.990	4.030	9.3	4.0
BaTiO_3 :Al,Mg	0.67		Trace ^e	0.46	3.990	4.032	11.4

^a Dopant concentrations (mol% relative to Ba^{2+}) determined by ICP analysis. ^b Lattice parameters estimated from 111, 002, and 200 reflections in XRD patterns. ^c Full width at half maximum (FWHM) values of the 312 cm^{-1} Raman band obtained by double-Gaussian fitting. ^d Specific surface area (SA) measured by Kr adsorption using the BET method. ^e Not detected (below the detection limit).

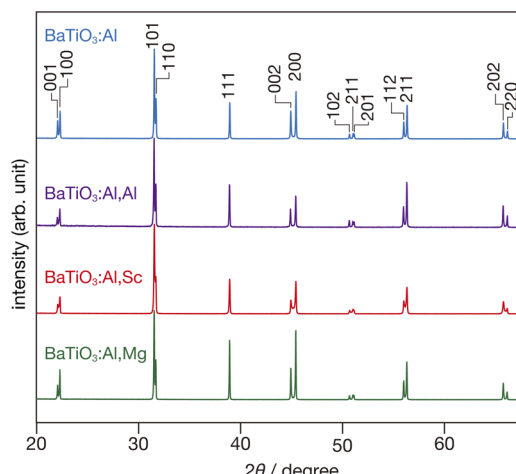


Fig. 2 X-ray diffraction (XRD) patterns of BaTiO_3 :Al, BaTiO_3 :Al,Al, BaTiO_3 :Al,Sc, and BaTiO_3 :Al,Mg powders.

among the BaTiO_3 -based samples cannot be attributed to macroscopic lattice distortion. Instead, the observed activity enhancement upon Sc^{3+} and Mg^{2+} doping is more likely related to local structural perturbations, defect formation, and electronic effects associated with the dopant ions, rather than changes in the average crystal lattice constants. Such effects may include modification of carrier generation and separation efficiencies, as well as suppression or activation of defect-mediated recombination pathways.

Fig. 3 shows diffuse reflectance (DR) spectra of the flux-treated samples. All the samples exhibited a sharp absorption edge near 400 nm. However, BaTiO_3 :Al and BaTiO_3 :Al,Al displayed pronounced Urbach tails extending into the visible region, indicative of band-edge disorder and high defect densities. For comparison, the DR spectrum of BaTiO_3 prepared by the SSR method (Fig. S1) showed a clean band edge without tailing, confirming that the Urbach tail observed in the Al-doped samples originates from Al-induced lattice disorder rather than from the intrinsic electronic structure of BaTiO_3 . The absorption edge of BaTiO_3 :Al,Sc was further analysed using Tauc plot analysis,¹⁷ assuming an indirect allowed transition, as commonly applied in previous optical studies (inset in Fig. 3). The estimated optical band gap of 3.16 eV, determined from the

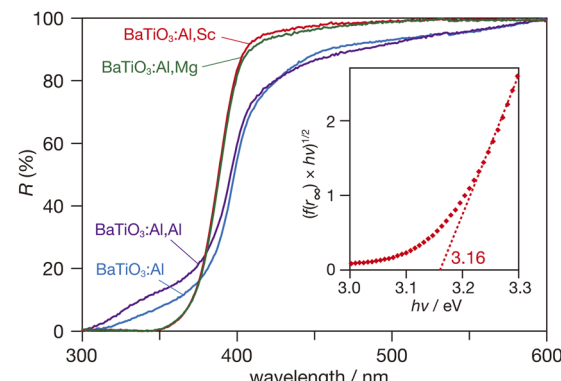


Fig. 3 Diffuse reflectance (DR) spectra of BaTiO_3 :Al, BaTiO_3 :Al,Al, BaTiO_3 :Al,Sc, and BaTiO_3 :Al,Mg samples. Inset: Tauc plot for the BaTiO_3 :Al,Sc sample assuming an indirect allowed transition.

x-axis intercept of the linear region, is in good agreement with the reported value for tetragonal BaTiO_3 at room temperature.¹⁸

Raman spectra of the samples (Fig. 4) exhibited a broad band centred at *ca.* 260 cm^{-1} , a sharp peak at *ca.* 312 cm^{-1} , representative of tetragonality strength in BaTiO_3 , an asymmetric broad band near 510 cm^{-1} , and a weak broad band around 715 cm^{-1} , consistent with reported spectra for BaTiO_3 .¹⁹ While the overall spectral shapes were similar, the 312 cm^{-1} peak

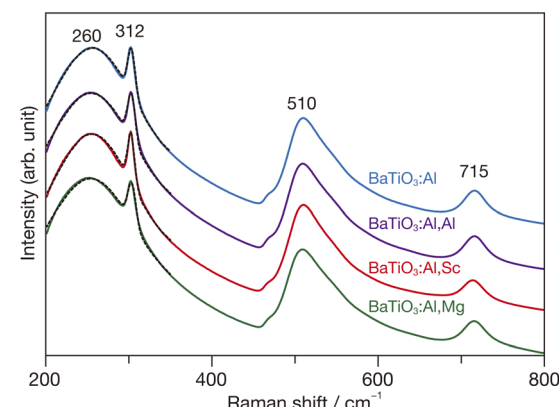


Fig. 4 Raman spectra of BaTiO_3 :Al, BaTiO_3 :Al,Al, BaTiO_3 :Al,Sc, and BaTiO_3 :Al,Mg samples. Dotted lines in $200\text{--}350\text{ cm}^{-1}$ range denote fitting curves obtained by double-Gaussian fitting.



appeared relatively sharper for the $\text{BaTiO}_3:\text{Al,Sc}$ sample compared with the others. To verify this observation, the spectra in the $200\text{--}350\text{ cm}^{-1}$ range were fitted using a double-Gaussian function, and the FWHM values of the 312 cm^{-1} peak were extracted and are summarized in Table 1. The results confirmed that the $\text{BaTiO}_3:\text{Al,Sc}$ sample exhibited the smallest FWHM, while the $\text{BaTiO}_3:\text{Al,Mg}$ sample showed a comparatively large FWHM. As reported previously,^{19b} Raman band width is inversely correlated with phonon lifetime, and accordingly, the observed sharpening indicates an increased phonon coherence length. Longer coherence lengths are generally associated with lower local defect densities, suggesting that $\text{BaTiO}_3:\text{Al,Sc}$ contains fewer defects relative to the other samples. In contrast, the broader peak of $\text{BaTiO}_3:\text{Al,Mg}$ reflects a shorter coherence length and thus a higher defect density. Although $\text{BaTiO}_3:\text{Al,Mg}$ exhibits a broader Raman band, indicating a higher overall defect density, its relatively weak Urbach tail (Fig. 3) suggests that many of these defects are shallow and less detrimental to carrier transport. Therefore, partial defect tolerance likely contributes to the moderate yet distinct photocatalytic activity of $\text{BaTiO}_3:\text{Al,Mg}$ compared with $\text{BaTiO}_3:\text{Al}$ and $\text{BaTiO}_3:\text{Al,Al}$.

As shown in Fig. 5, FE-SEM images of the flux-treated samples revealed clear morphology-dependent trends. $\text{BaTiO}_3:\text{Al}$ consisted of highly inhomogeneous particles with irregular shapes and rough surfaces. $\text{BaTiO}_3:\text{Al,Al}$ contained predominantly large grains (*ca.* $10\text{ }\mu\text{m}$) but also an admixture of smaller particles, and the large grains exhibited notably rough,

pitted surfaces. In contrast, the codoped samples were more uniform and generally smaller in size. Particularly, $\text{BaTiO}_3:\text{Al,Sc}$ showed an order-of-magnitude reduction in particle size relative to $\text{BaTiO}_3:\text{Al}$ and smooth, well-crystallized facets. Although $\text{BaTiO}_3:\text{Al,Mg}$ became more uniform than $\text{BaTiO}_3:\text{Al}$ or $\text{BaTiO}_3:\text{Al,Al}$, its size suppression was less pronounced than in $\text{BaTiO}_3:\text{Al,Sc}$. Such Sc^{3+} -induced suppression of particle growth is consistent with observations in SrTiO_3 and CaTiO_3 .^{6,10}

BET surface area measurements (Table 1) supported these tendencies while also reflecting surface texture and size distributions: the surface areas followed the order $\text{BaTiO}_3:\text{Al,Sc} > \text{BaTiO}_3:\text{Al,Al} > \text{BaTiO}_3:\text{Al,Mg} > \text{BaTiO}_3:\text{Al}$. The appreciably large value for $\text{BaTiO}_3:\text{Al,Sc}$ reflects its pronounced particle-size suppression, leading to an increased external surface area. Although $\text{BaTiO}_3:\text{Al,Al}$ has larger average particles than $\text{BaTiO}_3:\text{Al,Mg}$, its BET area is slightly higher, which can be rationalized by the rough, bumpy surfaces of the large grains and the coexistence of smaller particles that together raise the accessible external area. Conversely, the more uniform but less size-suppressed $\text{BaTiO}_3:\text{Al,Mg}$ exhibits a smaller value than that for $\text{BaTiO}_3:\text{Al,Sc}$. These SEM/BET results indicate that Sc^{3+} codoping most effectively suppresses grain growth and improves surface quality, thereby increasing the density of accessible active sites, whereas Mg^{2+} codoping primarily homogenizes the particle size distribution but provides a weaker inhibition of crystal growth.

Furthermore, several diffraction peaks of the $\text{BaTiO}_3:\text{Al,Sc}$ sample (Fig. 2) exhibited slightly weaker relative intensities than those of the other samples, although all reflections remained sharp. This attenuation likely reflects the smaller crystallite size of $\text{BaTiO}_3:\text{Al,Sc}$ rather than reduced crystallinity. The smaller, more uniform particles observed by SEM and the increased surface area determined by BET analysis (Table 1) both support this interpretation. Such microstructural refinement, *i.e.*, fine, well-crystallized particles with enlarged surface area, provides more active sites and facilitates carrier separation, thereby accounting for the markedly enhanced photocatalytic activity of $\text{BaTiO}_3:\text{Al,Sc}$.

Apparent quantum yield performance and mechanistic considerations

The apparent quantum yields (AQYs) of the most active photocatalyst (*i.e.*, $\text{BaTiO}_3:\text{Al,Sc}$ loaded with $\text{Rh/Cr}_2\text{O}_3$ and CoOOH cocatalysts) reached 29.8% at 310 nm and 27.5% at 365 nm, marking the first report of significant AQY values for a BaTiO_3 -based photocatalyst. Table 2 compares these results with benchmark SrTiO_3 - and CaTiO_3 -based systems. While the AQYs of $\text{BaTiO}_3:\text{Al,Sc}$ remain lower than those of optimized SrTiO_3 (>90% at 365 nm) and CaTiO_3 (>70% at 310 nm), they represent a major advance given that BaTiO_3 has long been considered inactive. By contrast, $\text{BaTiO}_3:\text{Al}$ alone exhibited essentially zero AQY, underscoring the critical role of codoping in surpassing the intrinsic activity threshold. The relatively lower AQY of $\text{BaTiO}_3:\text{Al,Sc}$ compared with SrTiO_3 and CaTiO_3 can be attributed to the absence of well-developed crystal facets (Fig. 5d), which are known to promote anisotropic charge separation and

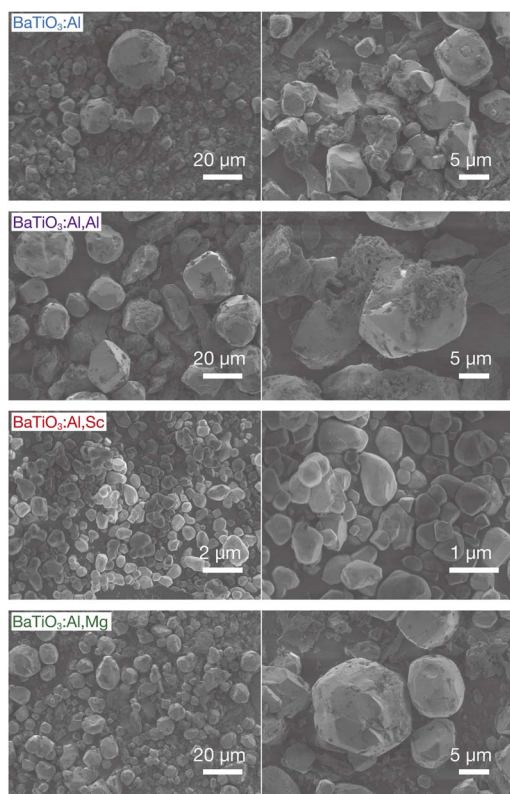


Fig. 5 SEM images of $\text{BaTiO}_3:\text{Al}$, $\text{BaTiO}_3:\text{Al,Al}$, $\text{BaTiO}_3:\text{Al,Sc}$, and $\text{BaTiO}_3:\text{Al,Mg}$ samples.



Table 2 Comparison of AQYs for overall water splitting over several benchmark titanate-perovskite photocatalysts under monochromatic UV irradiation^a

Sample	AQY (%)	Wavelength/nm	Reference
SrTiO ₃ :Al ^b	>96	365	3
SrTiO ₃ :Sc,Mg ^b	66	365	6
CaTiO ₃ :Al,Sc,Mg ^b	73.8	310	10
BaTiO ₃ :Al,Sc	29.8	310	(This work)
BaTiO ₃ :Al,Sc	27.5	365	(This work)

^a AQY measurements were performed after loading Rh/Cr₂O₃ and CoOOH cocatalysts for H₂ and O₂ evolution, respectively. ^b Titanate perovskites doped with various elements were obtained by high-temperature flux treatments.

accelerate surface redox processes. In addition, the present codoping strategy has not yet been optimized in terms of dopant ratios or flux treatment conditions. These factors indicate substantial room for further improvement, and ongoing efforts in our laboratory focus on morphology control, dopant optimization, and cocatalyst engineering.

Mechanistically, the activation of BaTiO₃ by Sc³⁺ codoping can be attributed to suppression of recombination-active defects and the resulting extension of carrier lifetimes. In Al³⁺-only samples, limited substitution and charge imbalance promote oxygen vacancy formation, which acts as recombination centres and accounts for their negligible activity. In contrast, BaTiO₃:Al,Sc exhibits markedly different behaviour. In SrTiO₃, Al³⁺ doping is known to enhance photocatalytic activity, suggesting that oxygen vacancies generated for charge compensation behave as shallow or electronically benign defects that do not significantly promote carrier recombination. By analogy, the lack of activity in Al-doped BaTiO₃ can be rationalized by considering its much larger lattice constant: the size mismatch between Ti⁴⁺ (0.0605 nm, CN = 6) and Al³⁺ (0.0535 nm, CN = 6) produces substantial local strain, which drives the formation of deep-level oxygen vacancies acting as non-radiative recombination centres. Codoping with Sc³⁺ (0.0745 nm, CN = 6) mitigates this lattice strain and provides local charge compensation, thereby suppressing the generation of deep-level vacancies and stabilizing the surrounding lattice. These effects manifest themselves in the narrower Raman peaks, reduced Urbach tails, smoother particle surfaces, and larger BET surface areas observed for BaTiO₃:Al,Sc compared with BaTiO₃:Al or BaTiO₃:Al,Mg. The stabilization of the local structure leads to prolonged carrier lifetimes, more efficient charge separation, and the highest photocatalytic activity among all BaTiO₃-based samples. Mg²⁺ codoping also improves activity, though less effectively, owing to less favourable charge balance and size mismatch. Further optimization of the codoping composition and detailed analyses of carrier lifetimes are currently underway to refine and extend these mechanistic insights.

Conclusions

This study demonstrates, for the first time, that BaTiO₃ can be activated as an efficient photocatalyst for overall water splitting through a codoping strategy. While BaTiO₃ doped only with Al³⁺

remained essentially inactive, codoping with Sc³⁺ together with crucible-derived Al³⁺ under flux conditions enabled significant activity, achieving apparent quantum yields of 29.8% at 310 nm and 27.5% at 365 nm, the highest values reported to date for BaTiO₃-based photocatalysts. These results overturn the long-standing perception of BaTiO₃ as unsuitable for photocatalytic water splitting. The enhanced performance originates from defect suppression and improved carrier dynamics induced by Sc³⁺ incorporation, which provides effective charge compensation and lattice stabilization. Mg²⁺ codoping also activated BaTiO₃, though less effectively, highlighting the critical role of ionic size and charge balance.

Overall, this work establishes codoping as a general design principle for unlocking latent activity in perovskite oxides, thereby broadening the family of viable photocatalysts for solar-driven H₂ production.

Author contributions

S. I. directed and led the research. K. T. performed photocatalytic experiments. K. T., R. T., A. Y. and Y. N. performed structural analyses. R. T., T. N., and K. H. performed compositional analyses. All the authors discussed the results. S. I. wrote the manuscript. All authors have given approval to the final version of the manuscript.

Conflicts of interest

The authors declare no conflict of interest.

Data availability

All data supporting the findings of this study are available within the article and/or its supplementary materials (SI). Additional datasets are available from the corresponding author upon reasonable request. Supplementary information: includes additional photocatalytic reaction data (time courses of H₂ and O₂ evolution) and diffuse reflectance spectra used for comparison of optical properties. See DOI: <https://doi.org/10.1039/d5se01323b>.

Acknowledgements

This work was supported by MEXT/JSPS KAKENHI Grant Number JP23K26767 and JSPS Bilateral Program Number JPJSPB120247415.

Notes and references

- (a) A. Kudo and Y. Miseki, *Chem. Soc. Rev.*, 2009, **38**, 253; (b) X. Tao, Y. Zhao, S. Wang, C. Li and R. Li, *Chem. Soc. Rev.*, 2022, **51**, 3561.
- (a) K. Domen, S. Naito, M. Soma, T. Onishi and K. Tamaru, *J. Chem. Soc. Chem. Commun.*, 1980, 543; (b) F. T. Wagner and G. A. Somorjai, *J. Am. Chem. Soc.*, 1980, **102**, 5494; (c) K. Sayama and H. Arakawa, *Chem. Lett.*, 1992, **21**, 253; (d)



S. Ikeda, K. Hirao, S. Ishino, M. Matsumura and B. Ohtani, *Catal. Today*, 2006, **117**, 343.

3 T. Takata, J. Jiang, Y. Sakata, M. Nakabayashi, N. Shibata and K. Domen, *Nature*, 2020, **581**, 411.

4 H. Nishiyama, T. Yamada, M. Nakabayashi, Y. Maehara, M. Yamaguchi, Y. Kuromiya, Y. Nagatsuma, H. Tokudome, S. Akiyama, T. Watanabe, R. Narushima, S. Okunaka, N. Shibata, T. Takata, T. Hisatomi and K. Domen, *Nature*, 2021, **598**, 304.

5 (a) A. Yamakata, H. Yeilin, M. Kawaguchi, T. Hisatomi, J. Kubota, Y. Sakata and K. Domen, *J. Photochem. Photobiol. C*, 2015, **313**, 168; (b) Y. Ham, T. Hisatomi, Y. Goto, Y. Moriya, Y. Sakata, A. Yamakata, J. Kubota and K. Domen, *J. Mater. Chem. A*, 2016, **4**, 3027; (c) T. H. Chiang, H. Lyu, T. Hisatomi, Y. Goto, T. Takata, M. Katayama, T. Minegishi and K. Domen, *ACS Catal.*, 2018, **8**, 2782.

6 S. Ikeda, R. Okamoto, A. Kimura, Y. Nakayasu, A. Yamakata, R. Tomizawa, T. Masuda and K. Nakatani, *Sustainable Energy Fuels*, 2024, **8**, 202.

7 (a) R. Konta, T. Ishii, H. Kato and A. Kudo, *J. Phys. Chem. B*, 2004, **108**, 8992; (b) Y. Sasaki, H. Nemoto, K. Saito and A. Kudo, *J. Phys. Chem. C*, 2009, **113**, 17536; (c) R. Niishiro, S. Tanaka and A. Kudo, *Appl. Catal. B*, 2014, **150–151**, 187; (d) H. Kato, Y. Sasaki, N. Shirakura and A. Kudo, *J. Mater. Chem. A*, 2013, **1**, 12327; (e) S. Suzuki, H. Matsumoto, A. Iwase and A. Kudo, *Chem. Commun.*, 2018, **54**, 10606; (f) K. Kaiya, Y. Ueki, H. Kawamoto, K. Watanabe, S. Yoshino, Y. Yamaguchi and A. Kudo, *Chem. Sci.*, 2024, **15**, 16025; (g) Y. Qin, Y. Wan, L. Xiang, T. Wang, D. Guo, F. Fang and K. Chang, *J. Catal.*, 2024, **437**, 115660.

8 Q. Wang, T. Hisatomi, Q. Jia, H. Tokudome, M. Zhong, C. Wang, Z. Pan, T. Takata, M. Nakabayashi, N. Shibata, Y. Li, I. D. Sharp, A. Kudo, T. Yamada and K. Domen, *Nat. Mater.*, 2016, **15**, 611.

9 (a) H. Mizoguchi, K. Ueda, M. Orita, S. C. Moon, K. Kajihara, M. Hirano and H. Hosono, *Mater. Res. Bull.*, 2002, **37**, 2401; (b) K. Shimura and H. Yoshida, *Energy Environ. Sci.*, 2010, **3**, 615; (c) T. Kimijima, K. Kanie, M. Nakaya and A. Muramatsu, *Cryst. Eng. Commun.*, 2014, **16**, 5591; (d) J. Lin, J. Hu, C. Qiu, H. Huang, L. Chen, Y. Xie, Z. Zhang, H. Lin and X. Wang, *Catal. Sci. Technol.*, 2019, **9**, 336; (e) H. Yoshida, R. Yamada and T. Yoshida, *ChemSusChem*, 2019, **12**, 1958; (f) T. Soltani, X. Zhu, A. Yamamoto, S. P. Singh, E. Fudo, A. Tanaka, H. Kominami and H. Yoshida, *Appl. Catal. B*, 2021, **286**, 119899.

10 K. Takagi, T. Ota, K. Kato, R. Tomizawa, T. Nagano, K. Hayashi, A. Yamakata, Y. Nose, N. Machida and S. Ikeda, *ACS Appl. Energy Mater.*, 2025, **8**, 11961.

11 T. Ota, R. Tomizawa, T. Nagano, K. Hayashi and S. Ikeda, *Mater. Adv.*, 2025, **6**, 3455.

12 (a) M. Acosta, N. Novak, V. Rojas, R. Ullán and F. R. Castro, *J. Appl. Phys.*, 2017, **121**, 054102; (b) B. Jiang, J. Iocozzia, L. Zhao, H. Zhang, Y. Harn, Y. Chen and Z. Lin, *Chem. Soc. Rev.*, 2019, **48**, 1194.

13 (a) K. Maeda, *ACS Appl. Mater. Interfaces*, 2014, **6**(3), 2167; (b) W. Song, E. M. Lopato, S. Bernhard, P. A. Salvador and G. S. Rohrer, *Appl. Catal. B*, 2020, **269**, 118750; (c) S. Chandrappa, S. N. Myakala, N. A. Koshi, S. J. Galba, S.-C. Lee, S. Bhattacharjee, D. Eder, A. Cherevan and D. H. K. Murthy, *ACS Appl. Mater. Interfaces*, 2024, **16**, 8763.

14 (a) Y. Inoue, T. Niijima, Y. Asai and K. Sato, *J. Chem. Soc., Chem. Commun.*, 1992, 579; (b) Y. Inoue, *Energy Environ. Sci.*, 2009, **2**, 364.

15 Y. Hiramachi, H. Fujimori, A. Yamakata and Y. Sakata, *ChemCatChem*, 2019, **11**, 6213.

16 R. D. Shannon, *Acta Crystallogr., Sect. A*, 1976, **32**, 751.

17 J. Tauc, R. Grigorovici and A. Vancu, *Phys. Status Solidi B*, 1966, **15**, 627.

18 (a) Y. S. Lee, J. S. Lee, T. W. Noh, D. Y. Byun, K. S. Yoo, K. Yamaura and E. Takayama-Muromachi, *Phys. Rev. B: Condens. Matter Mater. Phys.*, 2003, **67**, 113101; (b) V. Mishra, A. Sagdeo, V. Kumar, M. K. Warshi, H. M. Rai, S. K. Saxena, D. R. Roy, V. Mishra, R. Kumar and P. R. Sagdeo, *J. Appl. Phys.*, 2017, **122**, 065105.

19 (a) U. D. Venkateswaran, V. M. Naik and R. Naik, *Phys. Rev. B: Condens. Matter Mater. Phys.*, 1998, **58**, 14256; (b) A. Gajović, J. V. Pleština, K. Žagar, M. Plodinec, S. Šturm and M. Čeh, *J. Raman Spectrosc.*, 2013, **44**, 412; (c) D. Caruntu, T. Rostamzadeh, T. Costanzo, S. S. Parizi and G. Caruntu, *Nanoscale*, 2015, **7**, 12955.

